IOP Publishing | Royal Swedish Academy of Sciences Physica Scripta

Phys. Scr. **T171** (2020) 014049 (8pp) https://doi.org/10.1088/1402-4896/ab51f4

# Fuel inventory and impurity deposition in castellated tungsten tiles in KSTAR: experiment and modelling

**Sunwoo Moon[1,4], Eunnam Bang[2], Per Petersson[1], Dmitry Matveev[3], Suk-Ho Hong[2], Andreas Kirschner[3] and Marek Rubel[1]**

[1] KTH Royal Institute of Technology, 100 44 Stockholm, Sweden
[2] National Fusion Research Institute, Daejeon, Republic of Korea
[3] Institut für Energie und Klimaforschung—Plasmaphysik, Forschungszentrum Jülich, 52425 Jülich, Germany

E-mail: sunwoo@kth.se

Received 19 June 2019, revised 21 October 2019
Accepted for publication 28 October 2019
Published 6 March 2020

**Abstract**

Plasma-facing components have castellated structure for thermo-mechanical durability and integrity under high heat flux loads. However, fuel co-deposition in the grooves of the castellation may enhance fuel retention. In KSTAR, castellated tungsten tiles were tested to investigate the impact of tile shaping and misalignment on the retention. The tiles with poloidal and toroidal gaps of 0.5 mm were exposed at the divertor during a whole campaign encompassing 4364 s of plasma operation. Surfaces inside the gaps were analysed by means of $^3$He-based micro-NRA, ERDA and PIXE. Modelling of carbon deposition was performed with the impurity transport code 3D-GAPS assuming impurity penetration along the magnetic field lines with plasma-wetted areas defined by simple geometrical shadowing. The main deposited element is carbon with different concentration at the entrance of the groove, dependent on the tile shaping: $6 \times 10^{17}$ cm$^{-2}$ for a chamfered and misaligned gap and up to $283 \times 10^{17}$ cm$^{-2}$ for a flat and aligned gap. The deposition patterns are exponentially decreased to 4–10 $\times 10^{16}$ cm$^{-2}$ inside the gap. Deuterium concentration in the gaps described above ranges, respectively, from $2 \times 10^{17}$ cm$^{-2}$ to $50 \times 10^{17}$ cm$^{-2}$ at the top of the groove and decreases to 1–4 $\times 10^{16}$ cm$^{-2}$ following the carbon deposition trends. The highest carbon and deuterium densities are measured at the plasma-exposed side of the flat tile and aligned gap. Modelled deposition profiles reproduce qualitatively the experimentally observed trends.

Keywords: plasma-facing components, castellation, tungsten, KSTAR, deposition, fuel retention

(Some figures may appear in colour only in the online journal)

## 1. Introduction

Plasma-facing components (PFCs) in ITER will have a castellated structure in order to improve the thermo-mechanical durability and integrity under high heat flux loads [1]. However, such structure may act as a trap for deposited species, thus leading to enhanced fuel inventory in the grooves of the castellated tiles and between the tiles. Eroded and transported impurity atoms will be co-deposited with fuel species in the grooves, which may be considered as remote areas from the direct plasma flux. The surface area of the grooves in ITER will be approximately three times larger than the plasma-facing surface (PFS). In addition, the cleaning of remote areas by the current method is difficult [2]. This is related to nuclear safety, as the in-vessel fuel retention must not exceed 700 g [3].

Deposition and fuel retention in castellated structure were studied in several machines, TFTR [4], DIII-D, ASDEX

[4] Author to whom any correspondence should be addressed.

 

Upgrade (AUG) [5], TEXTOR [6–8], Tore Supra [9] and JET [2, 10, 11]. In AUG, a short-term experiment with castellated tiles with a 0.5 mm wide and 10 mm deep gap was performed. The maximum level of carbon ($7.5 \times 10^{16}\,\mathrm{cm}^{-2}$) was twice as high on the shadowed side of the entrance than on the plasma-exposed side of the gap. The carbon areal density decreased exponentially with a decay length of 0.6–1 mm to a level of $1 \times 10^{15}\,\mathrm{cm}^{-2}$. The deuterium concentration on the shadowed side is $4.6 \times 10^{16}\,\mathrm{cm}^{-2}$. The D/C ratio is in the range of 0.5–0.6 at the entrance and increases to about 1 deeper inside the gap. From 0.4%–4% of incident deuterium was retained at the gap surfaces. TEXTOR used two types of tiles (rectangular and roof-shaped) with a 0.5 mm gap width to investigate the effect of tile shaping on the deposition pattern and fuel retention in the gap. The results show that the poloidal gaps between shaped tiles have three times less deuterium compared to conventional tiles. Tore Supra studied a toroidal pump limiter that was exposed during the whole campaign. Deuterium distribution in the toroidal gap reached about $10^{19}\,\mathrm{cm}^{-2}$ near the edge and decreased by a factor of 15 to the deep part of the gap, whereas it increased at the bottom. Also, the peak values of the D/C concentration ratio were measured near the edge. In JET with the ITER-like wall (JET-ILW), the castellated beryllium limiters were exposed during the whole campaign. The deuterium deposition pattern has a fine structure: (i) low D content at the entrance of the gap, (ii) increasing concentration with a maximum $1 \times 10^{19}\,\mathrm{cm}^{-2}$ at about 0.5 mm, and (iii) a sharp decrease to values below $1 \times 10^{17}\,\mathrm{cm}^{-2}$. The estimated total retention in the castellation grooves is in the range of $0.7 \times 10^{22}$ to $14.6 \times 10^{22}$ atoms, corresponding to 0.02–0.5 g of deuterium. In summary, all studies on fuel retention have consistently shown a dramatic decrease of retention, by a factor of 20 or more, following the implementation of ILW [12–14] in comparison to JET with the carbon wall (JET-C). This in turn led to the decision to eliminate carbon PFCs in ITER [15].

The aims of the study reported in this paper were threefold: (i) to assess the impact of tile shaping and misalignment on the impurity deposition and fuel retention in castellated tungsten tiles; (ii) to model the deposition profiles in the castellation grooves; (iii) to verify results obtained previously in machines with short pulses on deposition and retention in castellated structures.

## 2. Experimental

The exposures were performed in the Korea Superconducting Tokamak Advanced Research (KSTAR), which is a medium-size tokamak with the major radius $R = 1.8$ m and the minor radius $a = 0.5$ m. The inner wall is fully covered by around 3400 graphite tiles. The toroidal magnetic field ($B_\mathrm{T}$) can reach up to 3.5 T, and the usual setting of $B_\mathrm{T}$ in the 2015 campaign was between 1.8 and 3.0 T. The maximum plasma current ($I_\mathrm{P}$) achieved is 1.0 MA with average line density up to $10^{19}\,\mathrm{m}^{-3}$, 500 kW ICRH at the frequency of 30 MHz (at $B_\mathrm{T} = 2$ T) is coupled, and the injected neutral beam injection (NBI) power is up to 5.0 MW with beam energy between 70 and 90 keV. The electron temperature ($T_\mathrm{e}$) is about 2–3 keV and the density ($n_\mathrm{e}$) is up to $5 \times 10^{19}\,\mathrm{m}^{-3}$. During the 2015 KSTAR campaign, most discharges were NBI-heated single-null H-mode with pulse lengths of approximately 10–15 s [16]. Figure 1(a) shows a poloidal cross-section and an example of the shot configuration.

In order to study the impact of tile shaping and misalignment on fuel retention, a number of castellated tungsten tiles were fabricated. Two sets of tungsten tiles were mounted on a stainless-steel base and installed at the central divertor of KSTAR, as shown in figures 1(b) and (c). Based on the ITER divertor mono-block design, the tiles were designed as cuboids with surfaces of 30 × 12 mm and 20 mm high. As shown in figure 2, the top 4–5 mm region is tungsten and then 2 mm pure copper as the intermediate layer based on a 13 mm plate made of copper-chrome-zirconium (CuCrZr) alloy. Some tiles have been chamfered, otherwise, other flat tiles shaped to fit the plasma field line curvature. Details have been given regarding the design in [16] and fabrication process in [17]. The tiles were installed with a perfect alignment and, for test purposes, with intentional misalignment. The misaligned tiles were taller than the neighbouring tiles and made shadowed areas from the plasma flux. In addition, the height of one side of the chamfered tiles was elevated to be 0.5 mm. The mentioned chamfer effect is considered as misalignment in this work.

The tungsten setup was located in the central divertor. As shown in figure 1(b), there are four lines of rectangular graphite tile lines named CD1 to CD4 in the poloidal direction. The setup was installed in CD2 marked as the red-dashed box, while in the blue-marked one there were two graphite tiles designed and installed in order to eliminate any shadowing of the tungsten tiles. By the X-point radial position control, the outer strike point was located as either CD1 or CD2 in the central divertor or on the outer divertor. Tungsten tiles were exposed to L- and H-mode plasma for 4364 s during whole 2015 KSTAR campaign (total plasma operation time is 12 411 s). The plasma edge was investigated by Langmuir probes during a previous campaign [18]. The central divertor temperature ($T_\mathrm{e}$) and density ($n_\mathrm{e}$) were calculated by scrape-off layer plasma simulation based on the midplane temperature. $T_\mathrm{e}$ was in the range 50–100 eV near the outer strike point and 1–10 eV in the private flux zone. The average values of the plasma parameters near the castellation were: $T_\mathrm{e} = 20$–$60$ eV, $n_\mathrm{e} = 8$–$25 \times 10^{17}\,\mathrm{m}^{-3}$ and $T_i = 1.5\ T_e$. The temperature of bulk tungsten was in the range 100 °C–500 °C, while the surface temperature increased to 1200 °C, according to the preliminary tests [19, 20]. The base temperature of the tiles that were not actively cooled between shots was in the range of 50 °C–80 °C.

### 2.1. Surface analyses

The analyses were performed on the eight selected tiles marked with an X in figures 1(c) and (d) at the Tandem Laboratory of the Uppsala University, using a micro-beam system for nuclear reaction analysis ($\mu$-NRA), particle-induced x-ray emission ($\mu$-PIXE) and time-of-flight heavy ion

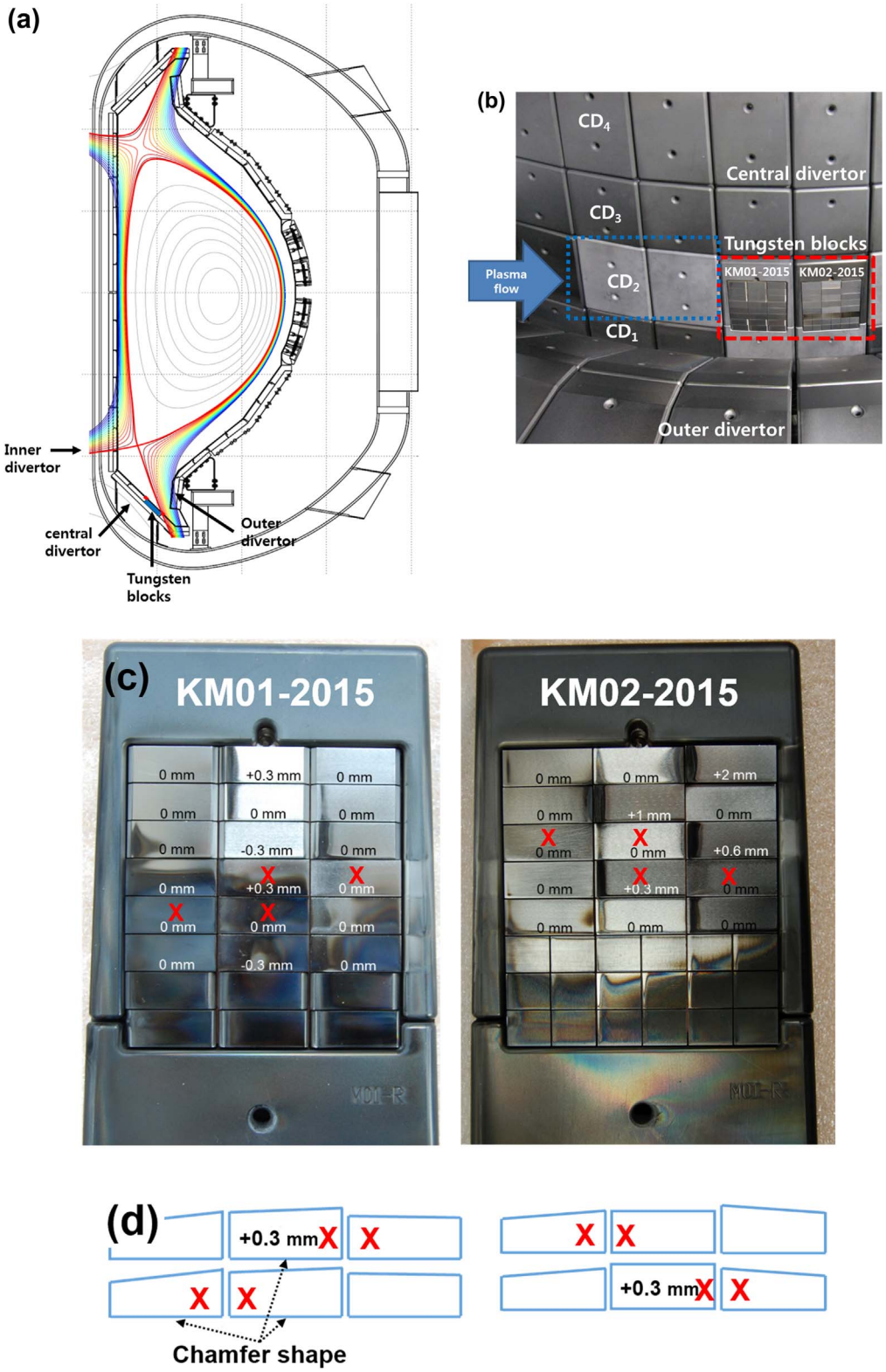


**Figure 1.** (a) Poloidal cross-section of KSTAR and an example of plasma configuration, (b) location of the tungsten tiles from the top view on the central and outer divertor, (c) two sets of the exposed castellated tungsten tiles in the cassettes, (d) drawing of selected tile shapes and misalignment. Eight selected tiles are marked with an X.

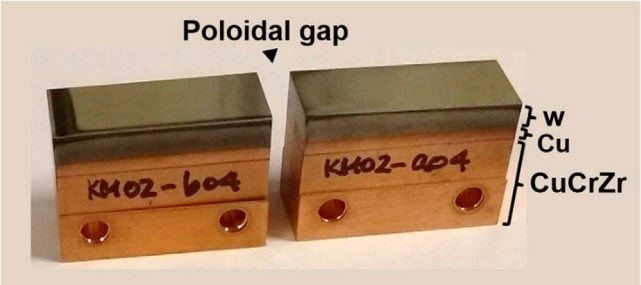


**Figure 2.** Tiles after exposure during the whole campaign in KSTAR. Narrow side is the poloidal gap and the wide side is the toroidal gap.

elastic recoil detection analysis (ToF-HIERDA). A 3 MeV $^3He^+$ ion beam was used for $^3He(d,p)^4He$ and $^3He(^{12}C,p)^{14}N$ reactions to quantify the deuterium and carbon content and their distribution. The energy of the emerging protons was measured by a 1500 $\mu$m thick active layer solid-state detector with a solid angle of 0.4 Sr and scattering angle of 165°. The detectors were covered with 30 $\mu$m aluminium foil to stop backscattered ions for detector protection. The beam spot was 20 × 50 $\mu$m and the beam current typically 0.25 nA. The focused ion beam was scanned to form images over areas of up to 2 × 1 $mm^2$ that were divided into 256 × 256 steps with a dwell time of 30 $\mu$s in each spot [21]. More details about the analytical setup are given in [22]. The analysis results have been integrated into one linear distribution profile for each side from 3–5 scanned areas. Due to the missing part of the scan, some profiles have discontinuity. From the energy distribution, the concentration of carbon and deuterium was calculated with the SIMNRA code [23]. The $\mu$-PIXE method with an x-ray detector at the angle of 45° was used for metal impurities. The metal concentrations were calculated by GUYLS based on the PIXE results. The PFSs of the tiles were measured by ToF-HIERDA with a 36 MeV $^{127}I^{8+}$ beam for the integrated carbon and deuterium amount at a certain depth.

### 2.2. Modelling

Modelling was performed at the Forschungszentrum Jülich with the 3D-GAPS impurity transport code for selected poloidal gaps [24]. Impurity penetration into gaps along magnetic field lines was assumed, so that the plasma-exposed areas were defined by simple geometrical shadowing. The gaps had different structure, as shown in figure 3(a) for the flat shape and perfectly aligned gap and in figure 4(a) for the chamfered 1° and misaligned 0.5 mm case. In the modelling, plasma parameters were used from a sample shot, since the implementation of a detailed campaign scenario is neither feasible nor possible. The input data were ion impact energy of 50 eV, uniform parallel ion flux ($\Gamma_{||}$) $10^{18}$ $D^+/cm^2/s$ with an impurity fraction of carbon ions of 1%, and a magnetic field line of 3° with respect to the flat-shaped surface. Additional parameters and conditions were assumed: (i) isotropic charge-exchange D neutrals (CXN) uniformly distributed over the gap entrance with the flux of 10% of the parallel $D^+$ flux, (ii) particles crossing the gap depth of 4.1 mm do not return and (iii) no D recycling. Reflected particles followed the cosine angular distribution with the energy and angle reflection coefficients according to the SDTrimSP fits. The physical sputtering data are from Eckstein [25] and the chemical erosion of carbon in the form of $CD_4$ with a constant erosion yield of 2% were used. The total simulation time was 1000 s. Steady-state integral deposition rates inside the gaps were achieved in all cases within 200 s, while the layer growth rate deep inside the gaps was very low.

## 3. Results and discussion

### 3.1. Poloidal gaps

Optical microscopy images in figures 3(b) and (c) show surfaces inside the gaps of the flat and aligned tiles. In figure 3(b), there is a plasma-shadowed side of the gap, i.e. the left side of the groove in figure 3(a), while in figure 3(c) is the side open to the magnetic field line. On both sides, one can perceive hue gradation in blackish deposition belts at the entrance to the gap: top 1 mm into the gap. There is also a very narrow and bold black belt near the top edge on the open side. These deposition patterns are reflected in the IBA results shown in figures 3(d) and (e). The main constituent in the co-deposited layer is carbon. The profile structure at the shadowed side indicates relatively low carbon content (about 6 × $10^{17}$ $cm^{-2}$) at the very entrance, which then increases to 1.13 × $10^{19}$ $cm^{-2}$ at about 0.4 mm into the gap followed by an exponential decrease to about 4 × $10^{16}$ $cm^{-2}$. The deuterium profile follows the carbon trend with the maximum value of 4.5 × $10^{18}$ $cm^{-2}$ and a decrease to 2 × $10^{16}$ $cm^{-2}$. The profile at the open area has a very sharp peak with the maximum carbon concentration of 2.83 × $10^{19}$ $cm^{-2}$ and deuterium 5 × $10^{18}$ $cm^{-2}$ at the position of the narrow black belt in a microscopy photo. Within 1.5 mm the concentration decreases to the level of 4.0 × $10^{17}$ $cm^{-2}$ of carbon and 3.7 × $10^{16}$ $cm^{-2}$ of deuterium. The ratio between the deuterium and carbon was calculated with a fitting curve value of the analysis results, since the ratio had high fluctuation when it was directly calculated by measurement profiles. The D/C ratio was 0.3–0.5 within 0.5 mm from the top and decreased to 0.2 at the shadowed side. At the open side it was 0.1 at the top, increasing to a maximum value of 0.6 at 0.6 mm and decreasing to less than 0.1 from 1.5 mm.

Modelling was done for the geometry shown in figure 3(a). As stated in section 2.2, the flux of deuterium CXN was assumed at the level of 10%. Most probably, the possible range of the effective CXN flux is smaller and the impact of re-erosion by CXN is over-estimated in the model. Quantitative comparison between the NRA and modelling results is not possible. However, the main features of the deposition profile are fairly well reflected by modelling: the same level of deposition on two sides, broader decay length in the flat-type gap and a sharp peak at the open side. The width of that sharp peak in the modelling clearly matches the plasma-exposed area (about 25 $\mu$m) at the open gap side.

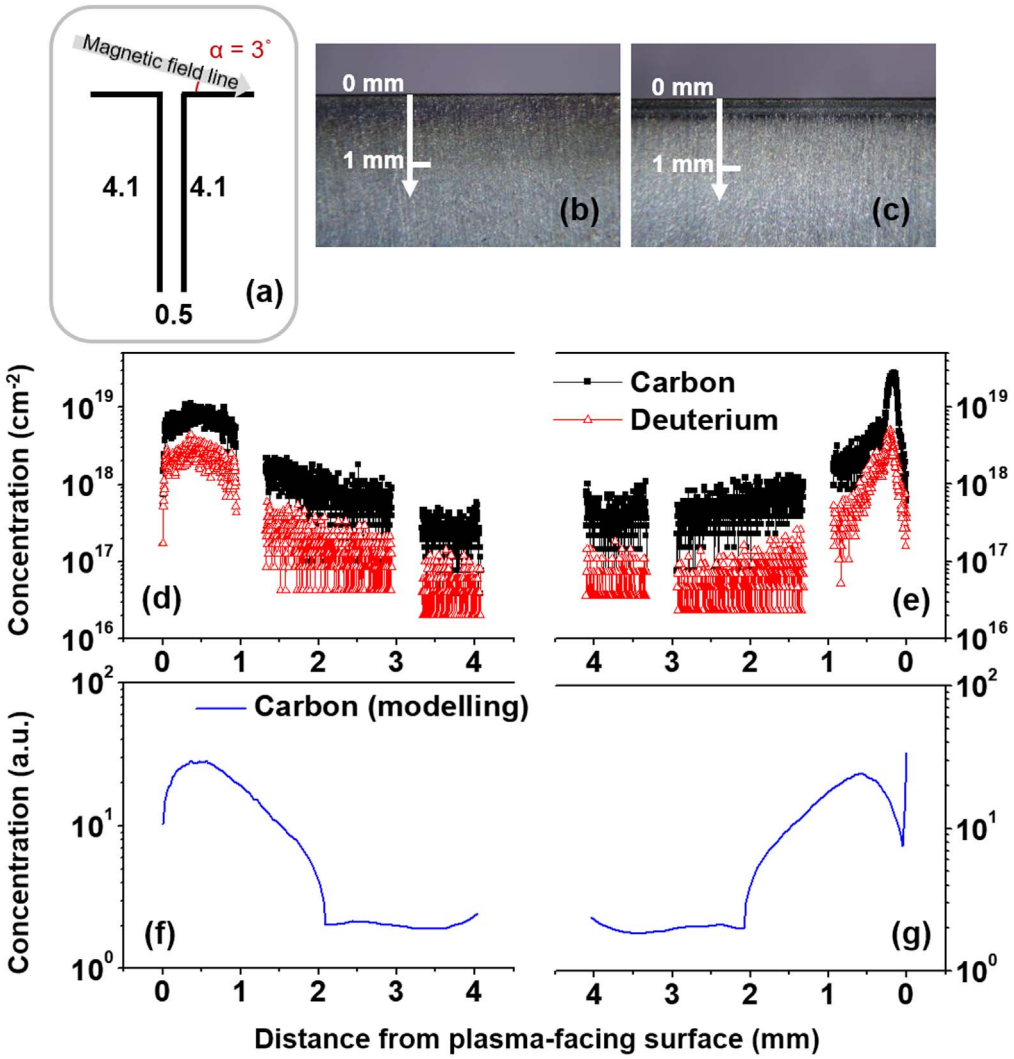


**Figure 3.** (a) Geometry of the flat and aligned gap for modelling. Left side is shadowed and the right is open to the magnetic field line. Optical microscopy images of surfaces in the poloidal gap: (b) shadowed side, (c) open side. Carbon and deuterium deposition profiles determined with NRA: (d) shadowed side, (e) open side. Modelling of carbon deposition profiles: (f) shadowed side, (g) open side.

The chamfered and misaligned gap has a different deposition level and trend to that on the flat and aligned case. As shown in figure 4(b), the shadowed side has several features: (i) erosion at the top edge, (ii) bold black belt and (iii) hue gradation. The analysis results match this trend, as shown in figure 4(d). The amount of deposition increases exponentially from the entrance to the highest value of carbon at $2.0 \times 10^{18}\,\mathrm{cm}^{-2}$ and deuterium at $4.9 \times 10^{17}\,\mathrm{cm}^{-2}$ at about 0.2–0.3 mm from the PFS and then decreases within 0.5 mm into the groove to $1.0 \times 10^{16}\,\mathrm{cm}^{-2}$ (carbon) and only $5.0 \times 10^{15}\,\mathrm{cm}^{-2}$ (deuterium) into the groove. The D/C ratio of the shadowed side is about 0.2 near the top and decreases to 0.1 after 1 mm, whereas it decreases to over 0.3 in the whole range at the open side. The modelling result, as shown in figure 4(f), has the same trend and the decay length of 0.5 mm on the shadowed side. In contrast, the open side has the highest value at the top edge. The gradation of about 1 mm from the groove entrance in figure 4(c) is confirmed by NRA: carbon and deuterium decrease exponentially in about 1 mm in figure 4(e). In summary, the chamfered gap has less deposition than that for the flat and aligned case.

Figure 5 shows the distribution of metallic impurities in the groove of the chamfered and misaligned gap. The Fe and Cr deposition trends follow those of carbon and deuterium in figure 4(d). The greatest value at the entrance is $2.5 \times 10^{17}$ Fe $\mathrm{cm}^{-2}$ and $8.0 \times 10^{16}$ Cr $\mathrm{cm}^{-2}$, and then one observes a decrease two orders of magnitude deeper into the gap. The metal sources in KSTAR are structural parts and diagnostics covers. Nickel has also been measured, but it is relatively uniform on all surfaces. Potential sources of nickel can be related to the brazing material of NiCuMn used in tile fabrication and accidentally melted armour in the NBI system during the campaign. The measurements clearly indicate that the concentrations of the respective metals are small.

### *3.2. Toroidal gap*

Plots in figure 6 show results for the (a) upper and (b) lower side of the toroidal gap. The tiles are chamfered in the

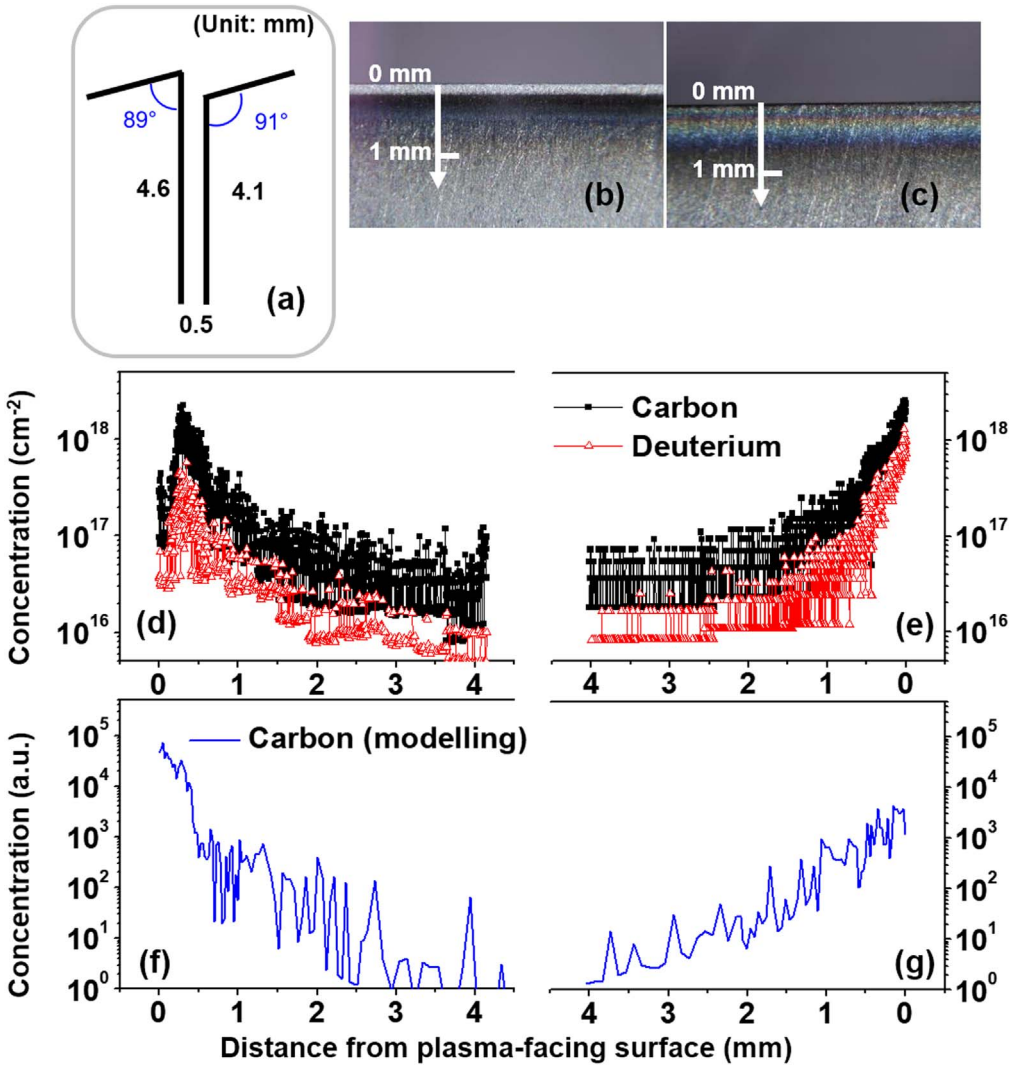


**Figure 4.** (a) Geometry of the chamfered and misaligned gap for modelling. Left side is shadowed and the right is open to the magnetic field line. Optical microscopy images of surfaces in the poloidal gap: (b) shadowed side, (c) open side. Carbon and deuterium deposition profiles determined with NRA: (d) shadowed side, (e) open side. Modelling of carbon deposition profiles: (f) shadowed side, (g) open side.

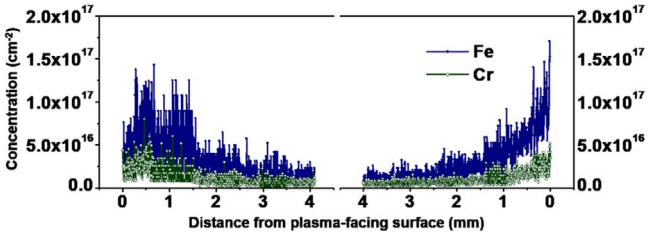


**Figure 5.** Deposition profiles of iron and chrome in the groove of the chamfered and misaligned gap.

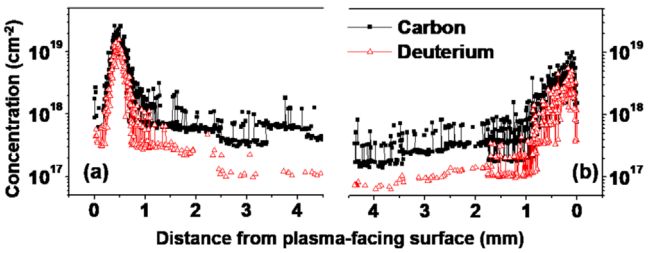


**Figure 6.** Carbon and deuterium profiles in the toroidal gap of (a) up- and (b) downside.

poloidal and flat in the toroidal direction. The selected toroidal gap has unintentional misalignment caused by poloidal misalignment: upper side is 0.3 mm higher than downside. The upper side of the toroidal gap was wetted by electrons. The deposition pattern is similar to the chamfered and misaligned case (figure 4), which also had a part wetted by electrons. The peak on the upper side surface is at 0.4 mm from the PFS with the carbon ($1.0 \times 10^{19}$ cm$^{-2}$) and deuterium ($5.6 \times 10^{18}$ cm$^{-2}$). In contrast, the lower side has a 1 mm broader decay pattern from the top edge.

In table 1, there are listed concentrations of carbon and deuterium on all analysed areas: in four types of poloidal gaps, one toroidal gap and PFS. On the PFS, carbon and deuterium were measured in only a few areas, while in the gaps this was done in 6–10 areas. This is justified by the fact that in the gaps there was a significant pattern indicating the

**Table 1.** Carbon and deuterium concentration of four poloidal gaps, one toroidal gap, and the PFS.

| Gap and surface | C ($10^{17}$ cm$^{-2}$) | D ($10^{17}$ cm$^{-2}$) |
|---|---|---|
| Poloidal gap (flat/flat, aligned) | 145.2 | 36.4 |
| Poloidal gap (flat/flat, misaligned 0.3 mm) | 36.1 | 6.2 |
| Poloidal gap (chamfered/chamfered, misaligned 0.5 mm) | 19.3 | 5.7 |
| Poloidal gap (chamfered/flat, misalignment 0.8mm) | 4.4 | 1.0 |
| Toroidal gap | 130.5 | 57.7 |
| PFS | 17.4 | 5.5 |

difference in deposition, whereas the appearance of the PFS was relatively uniform. Only the blackish deposited area (width 1–2 mm) on the PFS has four times higher carbon deposition than the other areas. The greatest C content is in the flat and aligned gap ($145.2 \times 10^{17}$ cm$^{-2}$), while the greatest D content is in the toroidal gap: $57.7 \times 10^{17}$ cm$^{-2}$, i.e. about 1.6 times higher than the maximum content found in the poloidal gap of the flat and aligned tile ($36.4 \times 10^{17}$ cm$^{-2}$). There is a sharp decrease of C ($36.1 \times 10^{17}$ cm$^{-2}$) and D ($6.2 \times 10^{17}$ cm$^{-2}$) content between that gap and the flat misaligned one and a further drop is observed for chamfered gaps in misaligned tiles. Eventually, the smallest C and D amounts were measured in the case of the biggest misalignment, $4.4 \times 10^{17}$ cm$^{-2}$ and $1 \times 10^{17}$ cm$^{-2}$, respectively, i.e. about 33–36 times smaller than on the flat aligned tile.

## 4. Concluding remarks

The work constitutes a contribution to the assessment of the relation between the arrangement of PFC tiles and fuel retention in the grooves of castellated structures. The main value is in an integrated approach to achieve as comprehensive as possible an outcome from a dedicated experiment performed in KSTAR: (i) careful design and precise manufacture of the tiles, (ii) definition of experimental condition, i.e. strike point position, (iii) *ex situ* analyses of all deposited species in an analytical system and (iv) modelling using a relevant code. As expected, carbon is the main deposited species, but the impact of the shaping and alignment/misalignment is distinct, taking into account the chamfer of only 1° and misalignment of up to 0.3 mm. It is remarkable that such apparently small modifications change the deposition by 50 times ($283 \times 10^{17}$ cm$^{-2}$ versus $6 \times 10^{17}$ cm$^{-2}$) with the greatest value in the flat and aligned tile setup, while a deliberate misalignment and/or chamfer have a positive impact resulting in the decreased deposition. Carbon fluxes drive co-deposition of deuterium with the deuterium-to-carbon concentration ratio in a range from 0.1–0.4, which is a range quite typical for carbon-wall machines [24].

From the quantitative point of view, integrated deuterium content in differently shaped gaps is to be considered: $3.64 \times 10^{18}$ in the flat aligned and $0.57 \times 10^{18}$, which corresponds to 12 and 1.9 $\mu$g, respectively, on the area of around 1 cm$^2$ (gap length × deposition width). These small amounts would lead to a huge retention if they are extrapolated to a full-scale operation in a carbon machine with millions of castellated tiles. However, with the elimination of carbon in next-generation devices [26], the risk of massive carbon-related retention would also be strongly reduced. In addition, other activities in KSTAR, such as glow discharge (GDC), can affect deposition and retention. However, only a minor contribution by GDC was observed in a previous experiment [27].

The most positive aspect is connected with the coherence of experimental and modelling data revealing one very positive trend: sharp decrease of deposition and related retention with the depth in the gap. The authors realise that the conclusions from this work would have been even clearer if the experiment had been limited only to the operation on the test tile. This would eliminate the risk that other factors (operation in the entire campaign) could have some impact on the final result. However, with a reasonable level of confidence, one can say that the observed results are related to the operation on the test tile. Otherwise, one would observe the same deposition on all tiles and gaps. These results of the carefully prepared KSTAR experiment consistently match observations that the deposition inside castellated metallic structure is very shallow [2, 10]. The data also indicate once again the need for tile shaping in a reactor class-machine.

## Acknowledgments

This work has been carried out within the framework of the EUROfusion Consortium and has received funding from the Euratom research and training programme 2019–2020 under grant agreement no. 633053. The views and opinions expressed herein do not necessarily reflect those of the European Commission. Work was also supported by the Ministry of Science, ICT, and Future Planning under KSTAR project (EN1901), under Non-ITER procurement (IN1910-2), and by the Swedish Research Council (VR), Grant 2015-04844.

## ORCID iDs

Sunwoo Moon https://orcid.org/0000-0002-0865-7387
Per Petersson https://orcid.org/0000-0002-9812-9296
Dmitry Matveev https://orcid.org/0000-0001-6129-8427
Andreas Kirschner https://orcid.org/0000-0002-3213-3225
Marek Rubel https://orcid.org/0000-0001-9901-6296

## References

[1] Loarte A *et al* 2007 *Nucl. Fusion* **47** S203
[2] Rubel M *et al* 2017 *Nucl. Fusion* **57** 066027
[3] Roth J *et al* 2008 *Plasma Phys. Control. Fusion* **50** 103001

[4] Hsu W L, Mills B E, Ehrhardt A B and Sun Y C 1989 *J. Vac. Sci. Technol.* A **7** 1065
[5] Krieger K *et al* 2007 *J. Nucl. Mater.* **363–365** 870–6
[6] Litnovsky A *et al* 2009 *J. Nucl. Mater.* **390–391** 556–9
[7] Litnovsky A *et al* 2011 *J. Nucl. Mater.* **415** s289–92
[8] Rubel M J *et al* 2004 *Phys. Scr.* **T111** 112
[9] Dittmar T *et al* 2009 *Phys. Scr.* **2009** 014027
[10] Rubel M J, Coad J P and Pitts R A 2007 *J. Nucl. Mater.* **367–370** 1432–7
[11] Coad J P, Rubel M and Wu C H 1997 *J. Nucl. Mater.* **241–243** 408–13
[12] Brezinsek S *et al* 2013 *Nucl. Fusion* **53** 83023
[13] Heinola K *et al Nucl. Fusion* **57** 086024
[14] Loarer T *et al* 2013 *J. Nucl. Mater.* **438** S108–13
[15] Merola M *et al* 2014 *Fusion Eng. Des.* **89** 890
[16] Hong S H *et al* 2016 *26th IAEA Fusion Energy Conf.* EX/P4-31 (https://nucleus.iaea.org/sites/fusionportal/Shared%20Documents/FEC%202016/fec2016-preprints/preprint0624.pdf)
[17] Hong S H *et al* 2015 *Fusion Sci. Technol.* **68** 36
[18] Bak J G *et al* 2015 *J. Nucl. Mater.* **463** 424–7
[19] Bang E N *et al* 2017 *Nucl. Mater. Energy* **12** 662
[20] Hong S H *et al* 2016 *Fusion Eng. Des.* **109–111** Part A 872–7
[21] Petersson P *et al* 2011 *J. Nucl. Mater.* **415** S761–4
[22] Bykov I *et al* 2015 *Nucl. Instrum. Methods Phys.Res.* B **342** 19–28
[23] Mayer M 1997 SIMNRA user's guide *Max-Planck-Institut für Plasmaphysik Report* IPP 9/113 (Garching: Max-Planck-Institut für Plasmaphysik)
[24] Matveev D *et al* 2010 *Plasma Phys. Control. Fusion* **52** 075007
[25] Eckstein W 2002 Calculated sputtering, reflection and range values *Max-Planck-Institut für Plasmaphysik Report* IPP 9/132 (Garching: Max-Planck-Institut für Plasmaphysik)
[26] Federici G *et al* 2001 *Nucl. Fusion* **41** 1967
[27] Hong S H *et al* 2013 *J. Nucl. Mater.* **438** S698–706